symmetry

MDPI

Article

Mechanical Behavior and Failure Mechanism of Rock–Concrete Composites Under the Coupling Effect of Inclined Interface Angle and Ground Temperature

Shiwei Liu [1,2,*], Jiaxin Zhao [1], Fang Cheng [1,*], Hao Yu [1] and Jiaqi Chen [1]

[1] College of Water Conservancy and Hydropower, Hebei University of Engineering, Handan 056038, China; jiaxiner99@163.com (J.Z.); a15354143796@163.com (H.Y.); m13229320988@163.com (J.C.)
[2] State Key Laboratory of Geomechanics and Geotechnical Engineering, Institute of Rock and Soil Mechanics, Wuhan 430071, China
* Correspondence: liushiwei@hebeu.edu.cn (S.L.); chengfang1021@163.com (F.C.)

Abstract: Surrounding rock and lining are composite structures with asymmetric mechanical properties. Understanding the mechanical properties and failure characteristics of rock–concrete composites is crucial for gaining insights into the mechanisms that induce disasters in deep-underground environments. Uniaxial compression and acoustic emission tests were conducted on rock–concrete composite specimens cured at temperatures of 20 °C, 40 °C, 60 °C, and 80 °C, with interface angles of 15°, 30°, 45°, 60°, 75°, and 90° respectively. The results indicated that the specimens' strength decreased at increasing geothermal temperatures. The composites with an 80 °C curing temperature and a 60° interface angle exhibited the lowest strength. A higher geothermal temperature significantly reduced the number of cracks in the concrete component during composite failure and mitigated the influence of the inclined interface angle. The failure modes of the specimens include axial penetration splitting, interface shear, Y-shaped fracture, and interface splitting–concrete shear failure. Finally, a model relating the strength of the rock–concrete composite to the inclined interface angle and the geothermal temperature was derived and verified against the experimental results with a relative error of 9.8%. The findings have significant implications for the safety and stability of tunnels in high-temperature conditions.

Keywords: rock–concrete composite; geothermal temperature; inclined interface angle; mechanical properties; failure mechanism

check for updates

Academic Editor: Theodore E. Simos

Received: 20 November 2024
Revised: 25 December 2024
Accepted: 29 December 2024
Published: 31 December 2024

Citation: Liu, S.; Zhao, J.; Cheng, F.; Yu, H.; Chen, J. Mechanical Behavior and Failure Mechanism of Rock –Concrete Composites Under the Coupling Effect of Inclined Interface Angle and Ground Temperature. *Symmetry* **2025**, *17*, 52. https://doi.org/10.3390/sym17010052

Copyright: © 2024 by the authors. Licensee MDPI, Basel, Switzerland. This article is an open access article distributed under the terms and conditions of the Creative Commons Attribution (CC BY) license (https://creativecommons.org/licenses/by/4.0/).

1. Introduction

Rock–concrete composites are commonly found in underground engineering activities, such as tunneling and mining [1–4]. The asymmetry of the mechanical properties of rock–concrete composite causes complexity in the mechanical behavior between the surrounding rock and lining. Many studies [5–12] have found that the rock–concrete interface is both the key to stress transmission and the weakest link in any support system, which often fails under the influence of stress disturbances, triggering engineering disasters or accidents. The mechanical behavior of the composite is the result of the combined impact of rock, concrete, and interface performance [13–19]. In-depth research on the mechanical behavior of rock–concrete composites and elucidating their failure mechanisms can help ensure engineering safety and stability.

The stress state near the interface between a concrete structure and surrounding rock is exceptionally complex owing to the potential coexistence of tensile, shear, and

compressive stresses [20–23]. This complex distribution of stress states often produces a loading direction that is neither parallel nor perpendicular to the interface. Scholars [24,25] refer to the inclined interface angle as the angle between the loading and interface normal directions. Numerous experiments and comparative analyses have found that the inclined interface angle is a critical factor affecting the static and dynamic mechanical properties of rock–concrete composites [26–28]. Saiang et al. [29] and Zhao et al. [30] respectively studied the mechanical properties of rock–concrete composites under uniaxial compression and triaxial compression conditions with an inclined interface angle of zero. Subsequently, Selçuk et al. [31] and Xu et al. [32] studied the influence of interface inclination angle on the strength and failure mode of composite materials under uniaxial compression conditions. In addition, Wu et al. [33], Shen et al. [34], and Dong et al. [35] respectively studied the effects of confining pressure, roughness, and water cement ratio on the mechanical behavior and failure mechanism of composites. However, most previous studies have not considered the influences of geothermal temperature on the mechanical properties and fracture characteristics of rock–concrete composites.

Notably, relevant data [36–40] indicate that the extent of tunnel engineering under high-temperature rock environments—found at deeper depths and in certain geological conditions—is increasing worldwide. Temperature primarily affects the hydration reaction process and hydration product yield of the cement inside concrete [41]. As the temperature increases, the cement hydration rate accelerates, the formation of hydration products increases, and the quantity of these products dispersed at the interface increases, enhancing the bonding strength across the interface [42]. However, when the temperature is too high, the cement hydration rate is too high and more hydration products are produced than those that can be effectively dispersed, decreasing the quantity of these products at the interface. Furthermore, the bonding strength across the interface also decreases under high-temperature conditions owing to the influence of temperature-induced stress [41,43]. Fang et al. [44], Tong et al. [45], and Zhang et al. [46] reported that an increase in temperature within a certain range could effectively improve the interfacial shear properties of rock–concrete composites. Furthermore, Su et al. [47] used high-temperature pretreatment to study the effects of interface roughness and temperature on the uniaxial compressive strength (UCS), acoustic emission (AE) characteristics, and failure modes of sandstone–concrete composites at an inclined interface angle of 90°.

To sum up, a large number of experiments have been conducted on the influence of temperature and interface inclination angle on the mechanical properties and failure characteristics of rock–concrete composites in the above-mentioned research, and fruitful results have been achieved. However most studies focus on the influence of interface inclination angle on the UCS of the composite, the influence of temperature on interface shear strength, and the influence of temperature and interface roughness on the UCS of the composite. There is relatively little research on the coupling effect of temperature and interface inclination angle. The deformation and failure of the interface between the concrete structures of deep tunnels and surrounding rock are the result of the coupling of geothermal temperature and inclined interface angle. Studying the coupled effects of interface inclination angle and temperature on the mechanical behavior and failure mechanism of rock–concrete can help reveal the deformation disaster mechanism of deep-buried high-temperature tunnels.

The present study aims to analyze the coupling effect of temperature and interface inclination angle on the mechanical behavior of rock–concrete composites. Therefore, this study prepared rock–concrete composite specimens with inclined interfacial angles ranging from 15 to 90° at curing temperatures ranging from 20 to 80 °C. A series of uniaxial compression tests were conducted to analyze the resulting fracture mode, stress–strain

response, peak strength, and elastic modulus of each specimen as well as the individual and cumulative AE event counts and *b*-value. Subsequently, the law describing the mutual influence of the geothermal temperature and inclined interface angle was explored, and a model correlating the UCS of the rock–concrete composite with the inclined interface angle and the geothermal temperature was established accordingly.

2. Experimental Program

2.1. Specimen Materials and Preparation

The composite specimens evaluated in this study comprised sandstone rock obtained from Shandong, China, and Portland cement concrete with a mix ratio of 1:0.82:1.43:0.44 (cement:medium sand:coarse aggregate:water) [48]. The cement used in this study was sourced from Taihang Company in Handan City, Hebei Province, China. The chemical, physical, and mechanical properties of the cement are shown in Table 1. The coarse aggregate comprised continuously graded crushed stone with particle sizes in the range of 5–10 mm, and the medium sand was dry river sand. The density, modulus of elasticity, compressive strength, and ultrasonic pulse velocity of the rock and concrete were determined using two standard 50 mm diameter, 100 mm high cylindrical specimens for each condition. Relevant tests were conducted following the American Society for Testing and Materials (ASTM) d2938-95 standard [49]. The results are shown in Table 2 and Figure 1. According to Figure 1, the UCS of the two sandstone samples is 141.47 MPa and 107.17 MPa, respectively, with an average value of approximately 124.32 MPa. According to Table 1, the density of concrete increases with the increase in curing temperature. This is mainly due to the increase in curing environment temperature, the acceleration of the cement hydration reaction, and the increase in hydration products. When the hydration products are generated too quickly and cannot be effectively dispersed, this leads to significant additional stress inside the concrete, exacerbates damage to the concrete, and causes the uniaxial compressive strength of the concrete to show a trend of first increasing and then decreasing; once the curing temperature exceeds 60 °C, the rate of decrease in wave velocity significantly accelerates.

Table 1. The chemical, physical, and mechanical characteristics of the cement used in the experiment.

Property	Value
Initial Setting Time (min)	180
Compressive Strength (MPa)	62.8
Tricalcium Sulfate Content (%)	2.4
Loss on Ignition (%)	2.0
Final Setting Time (min)	240
Cement Fineness (%)	0.4
Magnesium Oxide Content (%)	2.5
Standard Consistency Water Requirement (kg)	28.4

Table 2. Physical and mechanical properties of sandstone and concrete.

Material		Density (kg/m^3)	Modulus of Elasticity (GPa)	Compressive Strength (MPa)	Ultrasonic Pulse Velocity (km/s)
Sandstone		2405	23.07	124.32	3.73
Concrete cured at	20 °C	2209	6.38	51.95	4.08
	40 °C	2213	6.26	57.36	3.97
	60 °C	2245	6.64	74.09	3.74
	80 °C	2277	6.43	66.29	3.32

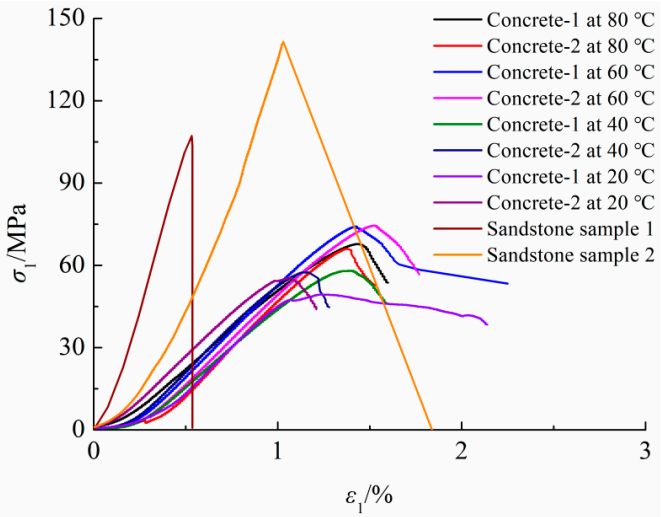


Figure 1. Stress–strain curves of the evaluated rock and concrete under uniaxial compression conditions.

The composite specimens were prepared by first grinding the ends of a sandstone cylinder and then cutting it open at the desired inclined interface angle to form a rock component at an inclined plane. The inclined cutting surface was polished flat with sandpaper, as shown in Figure 2. The rock components were then soaked in water for 24 h [50]. Each rock component was subsequently placed into a cylindrical polyvinyl chloride mold with an inner diameter of 50 mm and a height of 100 mm, and concrete was poured and evenly compacted into the remaining space. The cast composite specimens (as well as a set of standard concrete-only test specimens of the same size) were left to stand for 24 h and then placed in batches in a GDJS-225 high-temperature curing chamber at the desired geothermal temperature to cure for 28 d. The resulting rock–concrete composite specimens are shown in Figure 2.

When the loading direction is perpendicular to the rock–concrete interface, i.e., when the inclined interface angle is zero, the compressive strength of the composite is controlled by the material strength of either the rock or concrete as well as the interface morphology [29]. Selçuk et al. [31] found that when the inclined interface angle was zero, a rock–concrete composite specimen primarily underwent tensile splitting failure along its axial direction. Furthermore, curing temperature has been found to primarily affect the bond strength at the rock–concrete interface [43], and when the inclined interface angle was zero, the influence of the bond strength on the axial tensile splitting failure process was insignificant. Finally, Xu et al. [32] found that the failure mode and AE characteristics of a rock–concrete composite were consistent when the inclined interface angle was 0° and 15°. Therefore, inclined interface angles (β) of 15°, 30°, 45°, 60°, 75°, and 90° were applied in this study.

Numerous field investigations have shown that the surrounding rock temperature encountered during tunnel construction in high-temperature environments ranges from 30 to 110 °C [36–40]. Therefore, this study applied geothermal temperatures (T) of 20 °C, 40 °C, 60 °C, and 80 °C during curing under a constant humidity of 95%. The 20 °C temperature represents the natural ambient temperature and was applied as a control. Given that three specimens were prepared for each of the 24 evaluated conditions combining different β and T values, 72 composite specimens were tested in this study.

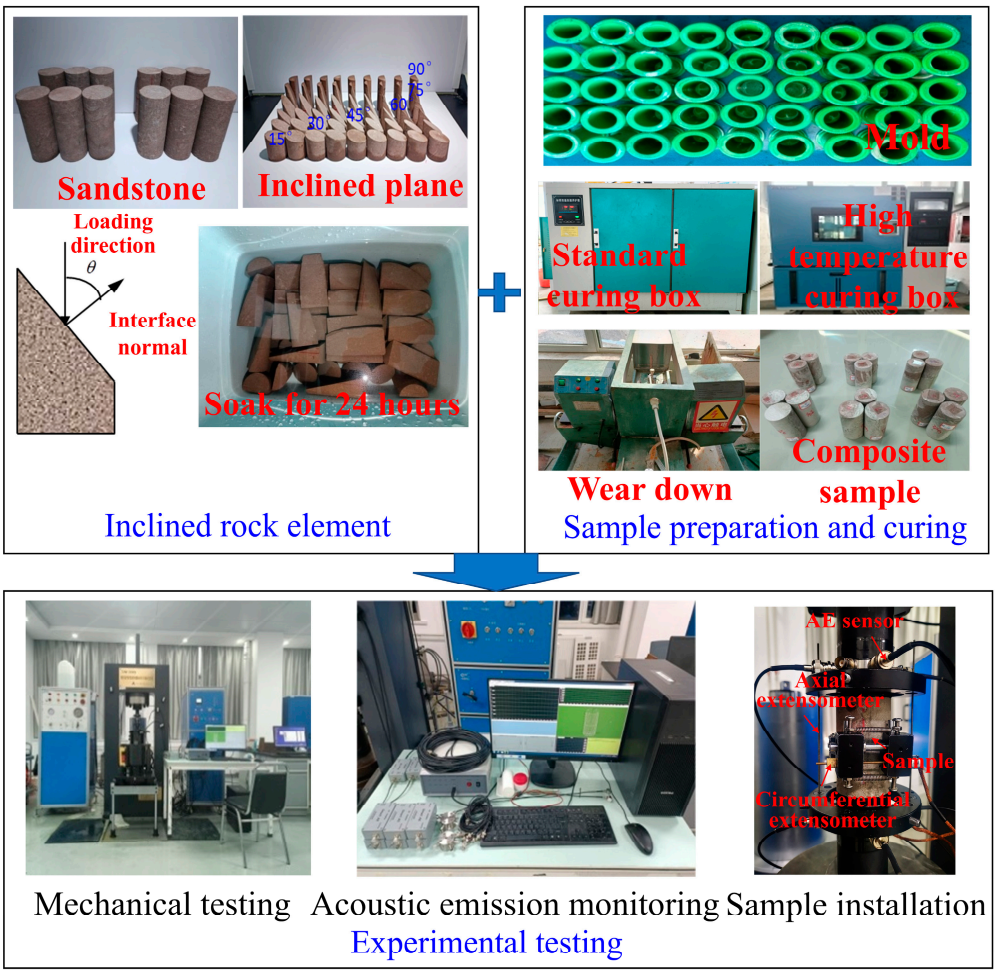


Figure 2. Testing process.

2.2. Testing Apparatus and Procedure

Uniaxial compression tests were conducted using a TAW-2000 rock testing machine at a deformation-controlled loading rate of 0.02 mm/min. Axial loading was applied until the specimen failed as per the ASTM D2938-95 standard [49]. AE is a technique based on real-time monitoring of internal stress waves in materials, capable of capturing acoustic signals generated by microscopic deformation or failure within the material. In this paper, the DS5 AE system from Soft Island Technology Co., Ltd. (Beijing, China) was used to extract AE signals, count AE events, and store data during the rock–concrete uniaxial compression tests. The arrangement of AE sensors is shown in Figure 2, with four sensors placed at both the upper and lower positions. The threshold value for the AE data acquisition system was set to 39 dB, and the minimum peak value was selected at 30 mV (equivalent to 49.5 dB). The parameters of the system were set as follows: Peak Definition Time (PDT) = 50 μs; Hit Definition Time (HDT) = 100 μs; and Hit Lockout Time (HLT) = 300 μs. The testing process is shown in Figure 2.

3. Results

3.1. Mechanical Properties

3.1.1. Stress–Strain Response Characteristics

The uniaxial compression stress–strain curves of the rock–concrete composite specimens with different inclined interface angles and temperatures are shown in Figure 3. According to the analysis of the graph, the uniaxial compression stress–strain curve of the rock–concrete composite can be divided into four stages: compression, linear elasticity,

yield, and post-peak. Before peak strength, all curves exhibit initial compaction and linear elastic stages with similar shapes. Notably, these stage characteristics are the same as those of the concrete-only specimens but differ significantly from those of the rock specimens.

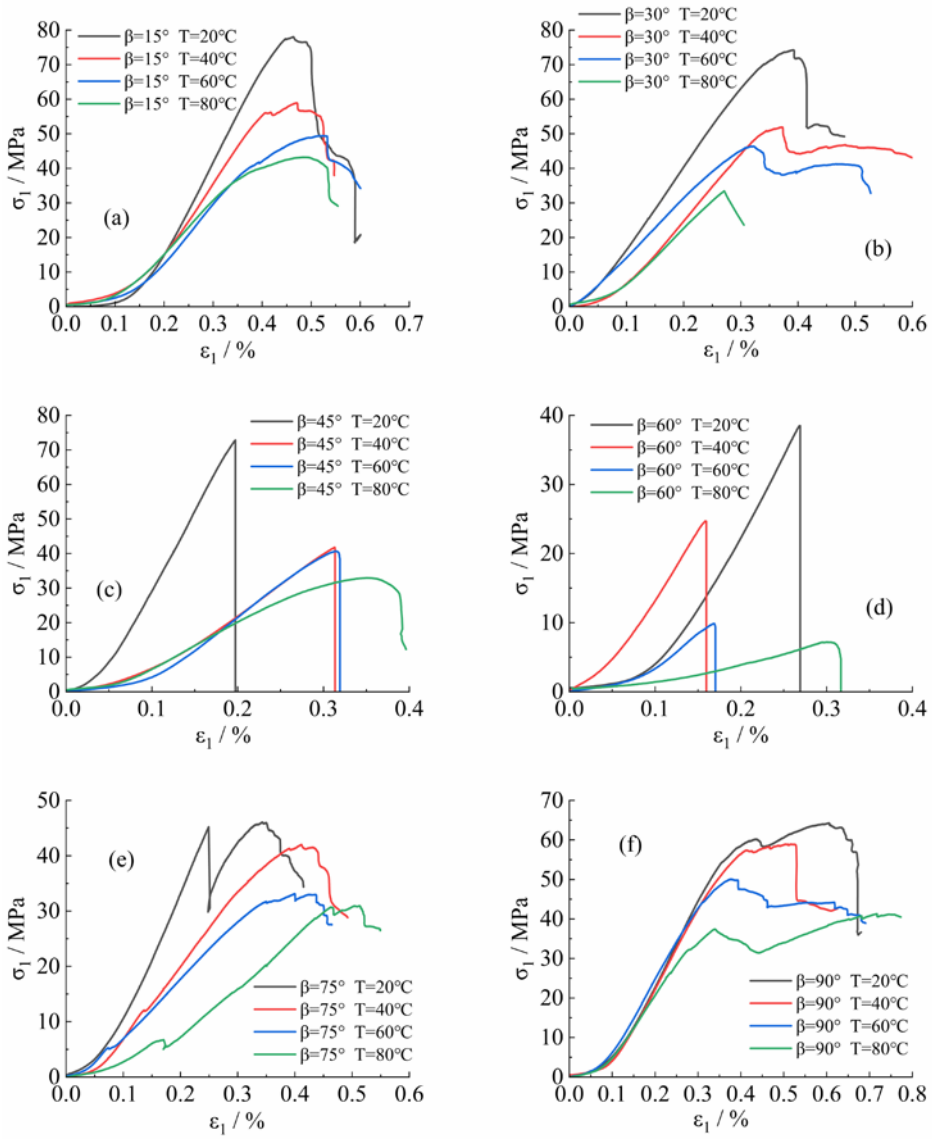


Figure 3. Stress–strain curves of rock–concrete composite specimens under uniaxial compression according to T when (**a**) β = 15°, (**b**) β = 30°, (**c**) β = 45°, (**d**) β = 60°, (**e**) β = 75°, and (**f**) β = 90°.

The yield segments of the composite specimen curves exhibit either obvious pre-peak hardening or no obvious pre-peak hardening according to β and T. Generally, the hardening trends are consistent with those of the corresponding concrete-only specimens. As shown in Figure 1, the lower the value of T, the more pronounced the pre-peak hardening in the concrete-only specimens. As shown in Figure 3a,b,e,f, the specimens with β = 15°, 30°, 75°, and 90° exhibited increasingly pronounced pre-peak hardening at increasing T, whereas Figure 3c,d show that there was no obvious pre-peak hardening in the specimens with β = 45° and 60° when T was 20 °C, 40 °C, or 60 °C; however, these specimens exhibited certain pre-peak hardening characteristics when T was 80 °C.

The post-peak stress–strain curves in Figure 3a,e indicate that the specimens with β = 15° and 75° cured at different T values all exhibit stress fluctuation softening followed by a severe drop in stress. As shown in Figure 3b, this behavior is also observed when β is 30° and T is 20 °C, but when T is 40 °C or 60 °C, post-peak softening is followed by

rehardening. The post-peak stress–strain curves in Figure 3c,d indicate that when β is 45° or 60°, the specimens cured at different T values all exhibit rapid stress drops. Finally, the post-peak stress–strain curves in Figure 3f show that a rapid drop in stress occurs when β is 90° and T is 20 °C or 40 °C; however, when T is 60 °C, initial stress fluctuation softening is followed by a drop in stress, and when T is 80 °C, the stress exhibits an initial peak, subsequent peak, and then continues to grow until reaching its final peak value. Thus, the post-peak stress–strain curves of rock–concrete composite specimens can be classified into three basic types manifested according to β and T, namely stress fluctuation softening, stress drop, and post-peak softening and rehardening.

3.1.2. Peak Strength

The variations in the UCS of rock–concrete composite with β and T are shown in Figure 4. Figure 4a exhibits a clear U-shaped trend at increasing β, which is consistent with existing research results [25]. Figure 4b shows a hump-shaped trend at increasing T, in which the UCS first increases and then decreases. When β is 60°, the UCS of the rock–concrete composite is relatively small. This may be because the substances involved in the hydration reaction at the rock–concrete interface were primarily provided by the concrete. When T was relatively low, the hydration products primarily filled the internal pores in the concrete, whereas when T was higher, the channels for dispersing these products were blocked, preventing them from being transported to the interface [43]. In addition, due to the difference in thermal expansion properties between rock and concrete, tensile stress is generated at the interface of the composite [41,43]. The higher the temperature, the greater the tensile stress at the interface of the composite and the more severe the damage to the composite. Thus resulted in a continuous decrease in the UCS of rock–concrete composite with increasing temperature.

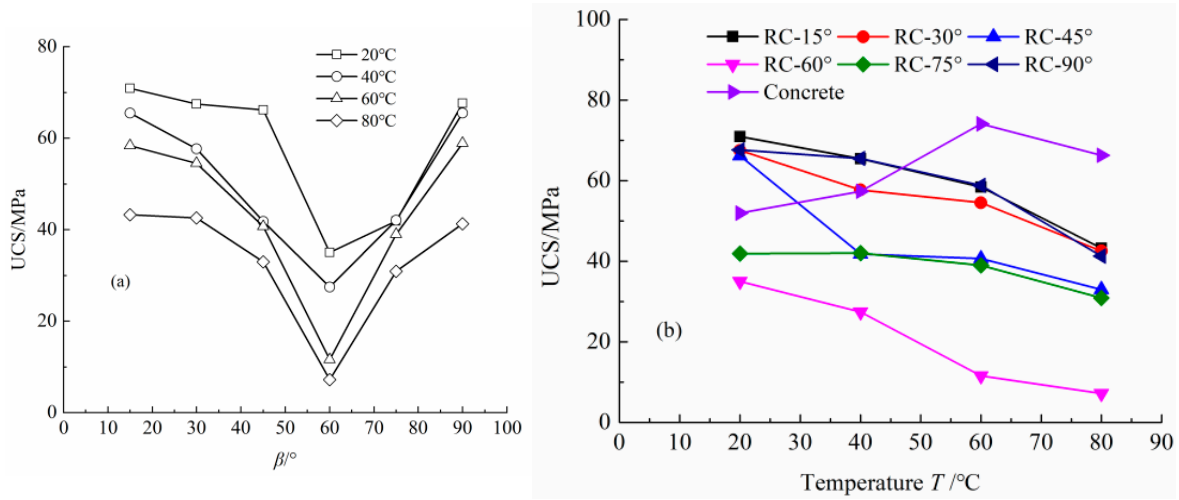


Figure 4. Changes in the UCS of rock–concrete composite specimens according to (**a**) β and (**b**) T.

3.1.3. Elastic Modulus

The variations in the elastic modulus of the rock–concrete composite (E_{rc}) with β and T are illustrated in Figure 5. Figure 5a shows that the elastic modulus of the rock (E_r) and concrete (E_{rc}) does not change significantly with T. The value of E_{rc} gradually decreases as T increases from 40 to 80 °C, but generally remains greater than E_c and less than the elastic modulus of the rock (E_r). When T is 20 °C, E_{rc} is equal to or greater than E_r. Furthermore, when β is 45° or 60°, the decrease in E_{rc} at increasing T values is large, and the influence of temperature on E_{rc} is most significant. Figure 5b shows that the increase in T causes the trend of the E_{rc} to change from fluctuating to U-shaped with the increase in β. When

T is 20 °C, the E_{rc} shows a trend of decreasing first, then increasing, and then decreasing again with the increase in β. When T is 40 °C, 60 °C, and 80 °C, the E_{rc} shows a trend of decreasing first and then increasing with the increase β.

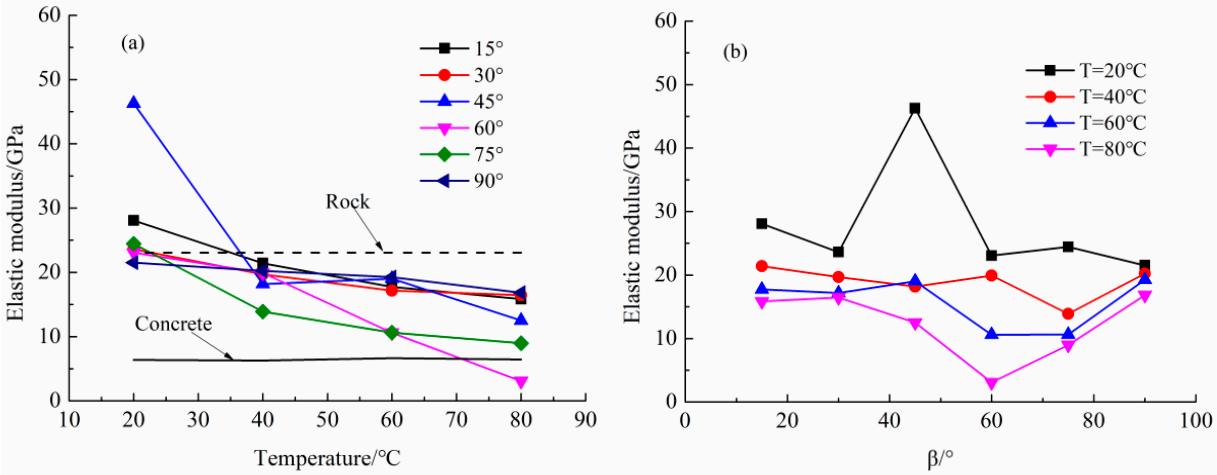


Figure 5. Changes in the elastic modulus of rock–concrete composite specimens according to (**a**) β and (**b**) T.

3.2. Failure Characteristics

3.2.1. Failure Modes

The failure modes of the composite specimens with different β values cured at different T values are shown in Figure 6. When β is 15° or 30°, tensile cracks first appear in the concrete component before they eventually occur in the rock and concrete. Furthermore, the number of tensile cracks in the concrete component gradually decreases as T increases, whereas the number of secondary cracks in the concrete component increases; this may be related to post-peak rehardening. The predominant failure mode of these specimens was axial penetration splitting. When β was small, the interface was under high normal stress and low shear stress, preventing interface failure.

As β increased to 45° and 60°, the normal stress on the interface decreased while the shear stress increased. When the interface shear stress reached the peak shear strength, the specimen underwent shear sliding failure along the interface, losing its load-bearing capacity and causing the stress–strain curve to exhibit an abrupt decrease, indicating elastic–brittle failure. Some specimens also exhibited edge spalling owing to local secondary fractures under these conditions.

When β increased further to 75°, the composite specimen exhibited Y-shaped failure characteristics. The failure of rock–concrete composites is manifested as shear failure along the interface, while the concrete components undergo splitting failure, with both failure surfaces exhibiting a Y-shaped characteristic.

When β increased further to 90°, the composite specimen exhibited characteristics of splitting failure along the interface and shear failure of concrete. The specimen undergoes splitting failure along the interface, while shear cracks occur in the concrete element. This is mainly due to the phenomenon of post-peak re-hardening during the loading process of the specimen, which also results in a significantly greater degree of damage to the specimen compared to other situations. After the sample undergoes splitting failure, the stress briefly drops, but the composite still has a certain bearing capacity, and the stress rises again under continuous loading. Due to the lower strength of concrete compared to rock, with continuous loading, the concrete undergoes further failure, resulting in more cracks.

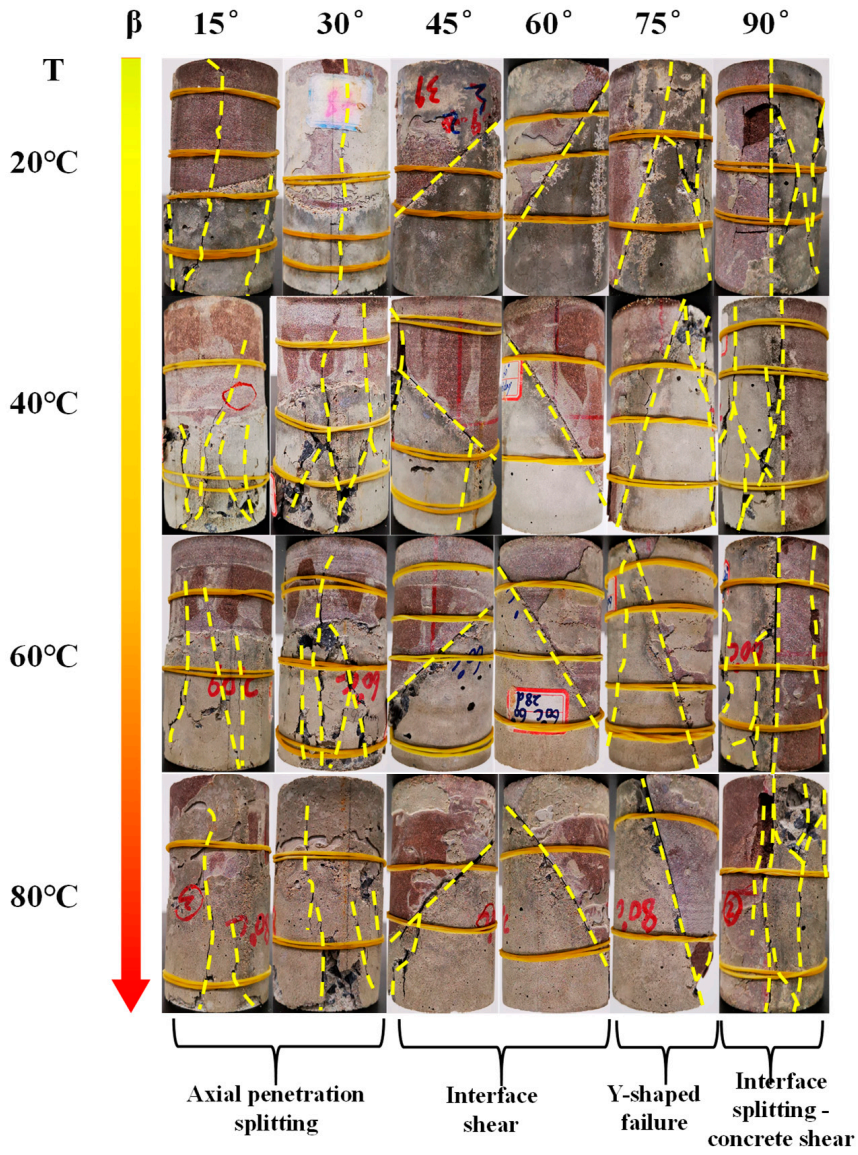


Figure 6. Failure modes of rock–concrete composite specimens.

In summary, increases in β and T caused the primary failure modes of the rock–concrete composite specimens to shift from axial penetration splitting of the composite and concrete component to interface shear failure, Y-shaped failure caused by interface shear, and concrete shear, Y-shaped failure caused by interface tension and concrete shear, and interface splitting–concrete shear failure. The failure modes of the composite specimen were primarily influenced by β, whereas an increase in T primarily decreased the number of cracks in the concrete and increased the concrete strength, exacerbating rock failure.

3.2.2. Individual and Cumulative AE Event Counts

The use of AE technology to acquire the energy signals released during the fracture of rock-like materials can reveal the various stages of crack development. This study monitored the AEs from rock–concrete composite specimens under uniaxial compression to obtain the evolution laws for the individual and cumulative AE event counts and thereby analyze the influences of β and T on the development of cracks in the specimens, as shown in Figures 7 and 8. In these figures, T_1 represents the compaction stage of the stress–time curve, T_2 represents the linear elastic stage, T_3 represents the plastic yield stage, and T_4 represents the post-peak stage.

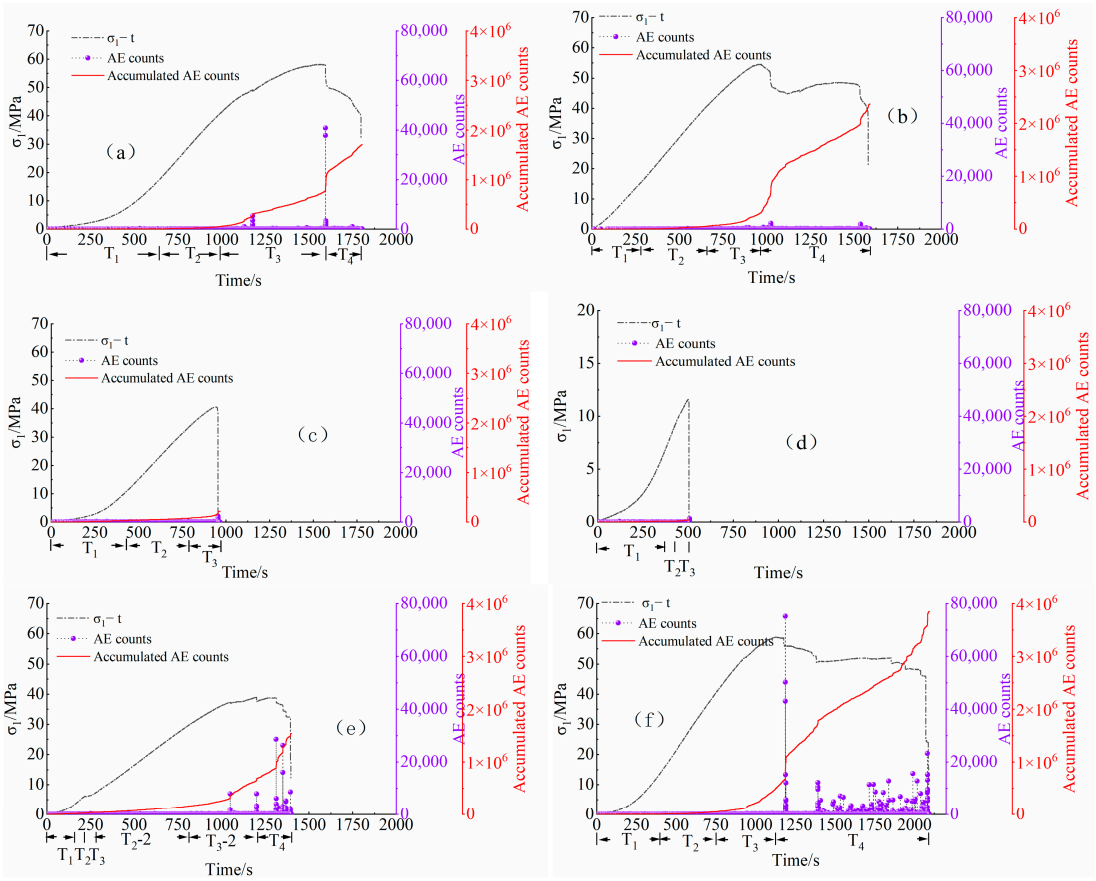


Figure 7. Individual and cumulative AE counts according to the stress in the composite specimens at T = 60 °C and (**a**) β = 15°, (**b**) β = 30°, (**c**) β = 45°, (**d**) β = 60°, (**e**) β = 75°, and (**f**) β = 90°.

As shown in Figure 7, the evolution laws of the individual and cumulative AE event counts during loading agreed with the stress–time curves. The individual AE event curves for specimens with β values of 15°, 30°, 75°, and 90° all reflect low-signal activity in Stages T_1 and T_2, a sudden increase in Stage T_3, and steady activity in Stage T_4; their cumulative AE event curves all exhibit steady low-speed growth accompanied by an unclear increase in event amplitudes in Stages T_1 and T_2, an accelerating increase in Stage T_3, followed by steady high-speed growth following the peak point in Stage T_4. These results indicate that specimens with these β values primarily experienced deformation owing to the closure of microcracks in the rock and concrete components during Stages T_1 and T_2; phenomena related to microcrack rupture and stable expansion in the rock, concrete, and interface were not evident. However, numerous microcracks exhibited unstable development and growth as the slip along the cracks increased during Stage T_3; as the loading continued further, the merging and penetration of these cracks gradually accelerated to form potential fracture surfaces. Finally, the specimen's damage increased continuously in Stage T_4, resulting in a large number of macroscopic cracks penetrating the specimen and causing it to break. However, when β = 45° or 60°, the cumulative AE event curve trends vary inconsistently and exhibit no stable increases in Stage T_4, indicating that the deformation and fracture of these specimens generally comprised the closure, propagation, and penetration of microcracks along the interface.

As shown in Figure 8, the individual AE event counts gradually decreased as T increased, reflecting a slowing crack propagation speed, and only the cumulative AE event curves for the β = 60° specimens exhibit notable deceleration. However, this deceleration gradually disappears at increasing T. Thus, an increase in T gradually weakened the

severity of microcrack expansion and development within the composite specimens and affected the variation in the microcrack expansion process along the interface.

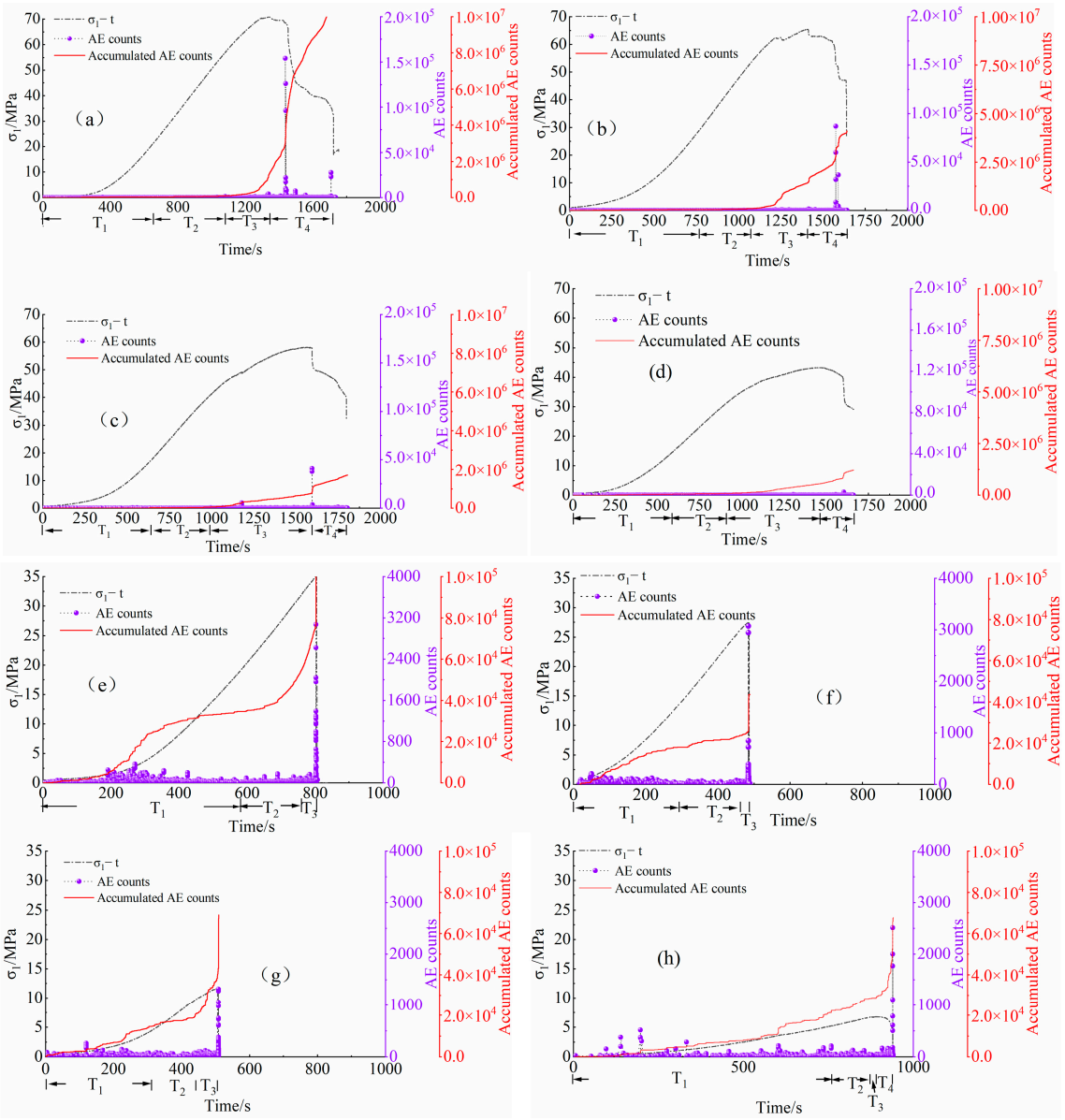


Figure 8. Individual and cumulative AE counts according to the stress in composite specimens with $\beta = 15°$ and β = 60° at (**a**) T = 20 °C β = 15°, (**b**) T = 40 °C β = 15°, (**c**) T = 60 °C β = 15°, (**d**) T = 80 °C β = 15°, (**e**) T = 20 °C β = 60°, (**f**) T = 40 °C β = 60°, (**g**) T = 60 °C β = 60°, and (**h**) T = 80 °C β = 60°.

3.2.3. Evolution of AE b-Value

The amplitude of an AE event represents its intensity (expressed in dB). The relationship between the cumulative frequency of the AE event amplitude and magnitude is reflected by the well-known Gutenberg–Richter equation [51], which is given by

$$\lg N = a - bM \tag{1}$$

where M is the magnitude of the event, which is typically calculated for AE tests by dividing the amplitude AdB of the AE event by 20, i.e., $M = AdB/20$, N is the cumulative number of events with a magnitude greater than M, a is a constant reflecting the event activity level at a specific time in a specific region. The b-value is an important parameter that characterizes the amplitude distribution of AE signals, commonly used to describe the relationship

between signal intensity and the frequency of event occurrence. The b-value typically reflects the distribution characteristics of microscopic damage during the material failure process. A higher b-value (close to 1) indicates a greater number of events occurring in the lower amplitude range (associated with small cracks or localized damage), while a lower b-value (close to 0) suggests that larger failure events (such as major cracks or macroscopic damage) are more prominent. As a parameter for describing the size distribution of AE events, the b-value provides physical insights into the characteristics and development trends of crack propagation and failure processes in rock mechanics. Monitoring and analyzing the changes in the b-value can help identify failure modes in rock materials, predict instability risks, and provide essential information for the assessment of rock mass stability and engineering safety management. Previous research results [52–55] have shown that (1) an increase in the *b*-value indicates an increase in the proportion of low-amplitude AE events, reflecting the dominance of small-scale cracks and vice versa; (2) the stable variation in the *b*-value means that the distribution of small- and large-amplitude AE events is relatively stable, reflecting a constant proportion of microcracks at different scales; and (3) a small change in the *b*-value indicates the slow development of microcracks, whereas a sudden change in the *b*-value indicates the unstable growth of microcracks. Thus, the size of and variation in the *b*-value are critical parameters reflecting the developmental state of the microscopic to macroscopic cracks in rock-like materials during loading.

The variation in the *b*-value with stress was estimated in this study using a running window of 500 events and a running step of 100 events under different β and T values, as shown in Figure 9. Furthermore, the *b*-value corresponding to the peak strength (the M point) was selected to analyze the influence of β and T as shown in Figure 10. Figure 9 indicates that the *b*-value was relatively large at the beginning of stress loading, suggesting that primarily small-scale microcracks were developing at this time. Subsequently, the *b*-value decreased slowly as the stress level increased and then decreased suddenly near M, reflecting the development of large-scale microcracks when the peak strength was approached, followed by the formation of macroscopic cracks that caused the composite specimen to break. This is consistent with previous research findings [52,53]. Regardless of T, the *b*-value typically decreased at increasing stress levels. When $\beta = 30°$, the variation in *b*-value with stress was relatively large when T was 40 °C or 80 °C but relatively small when T was 60 °C. This indicates that when $\beta = 30°$ and $T = 60$ °C, the distribution of crack development in the specimen was relatively uniform, with small- and large-scale cracks developing in approximately equal proportions.

As shown in Figure 10, both β and T had significant impacts on the AE *b*-value at the peak strength. The *b*-value at point M gradually increased with T, which is consistent with the findings of Ge et al. [55]. This indicates that under the same stress conditions, a higher T gradually increased the proportion of small-scale cracks developing in the specimens during failure. Furthermore, the *b*-value at point M first decreased, then increased as β increased; the *b*-value at the peak strength being significantly smaller for $\beta = 60°$ than for the other β values, indicating that this specimen exhibited a relatively higher proportion of large-scale cracks when damaged. Thus, under the same stress conditions, the specimen with $\beta = 60°$ was more likely to fail. This is consistent with the UCS results for the composite specimens.

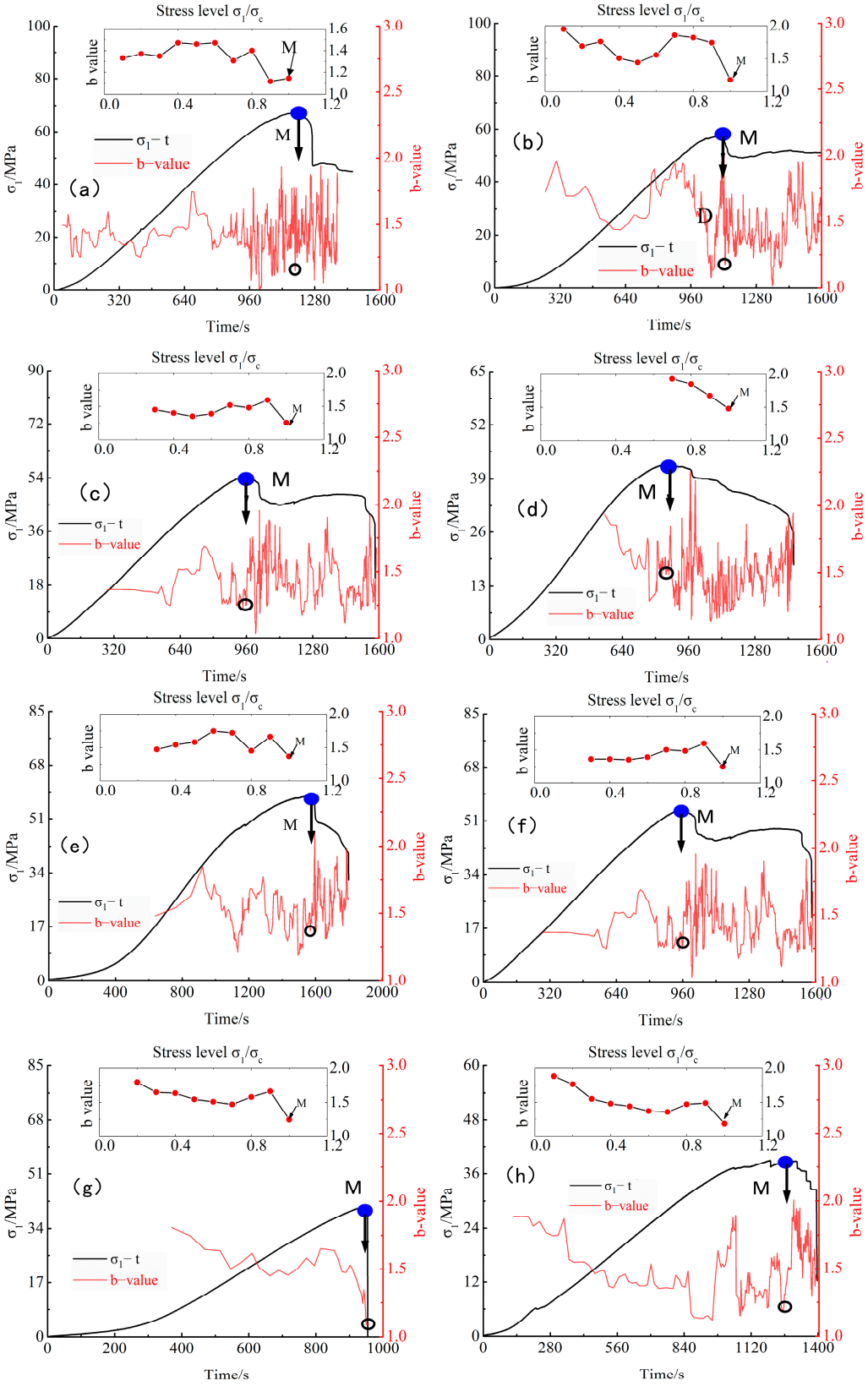


Figure 9. Evolution of AE *b*-values in rock–concrete composite specimens for (**a**) $\beta = 30°$ and $T = 20$ °C, (**b**) $\beta = 30°$ and $T = 40$ °C, (**c**) $\beta = 30°$ and $T = 60$ °C, (**d**) $\beta = 30°$ and $T = 80$ °C, (**e**) $\beta = 15°$ and $T = 60$ °C, (**f**) $\beta = 30°$ and $T = 60$ °C, (**g**) $\beta = 45°$ and $T = 60$ °C, and (**h**) $\beta = 75°$ and $T = 60$ °C.

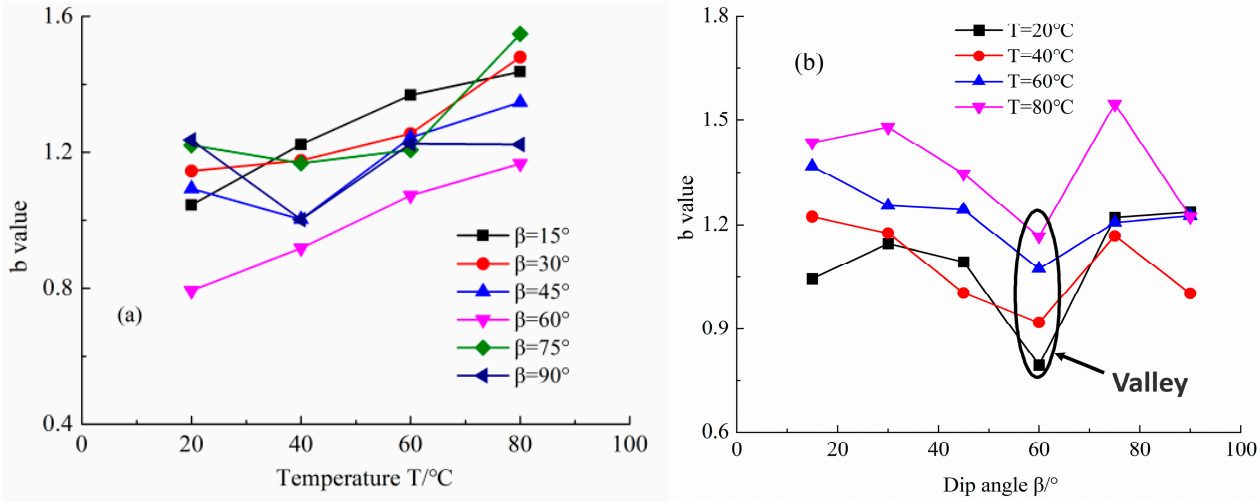


Figure 10. Effects of β and T on AE b-value for (**a**) T and (**b**) β.

4. UCS Model Based on β and T

At the same T, the ratio of the difference between the maximum and minimum composite specimen UCS values to the concrete-only specimen UCS value reflects the degree of influence of the inclined interface angle (*DIIA*). Figure 11a shows that the *DIIA* gradually decreased from 0.69 to 0.54 as T increased from 20 to 80 °C. However, the rate of decrease in the *DIIA* was significantly larger when T was greater than 60 °C, suggesting that an increase in T can effectively reduce the impact of β on the UCS of the rock–concrete composite, and the higher the T, the more pronounced this reduction.

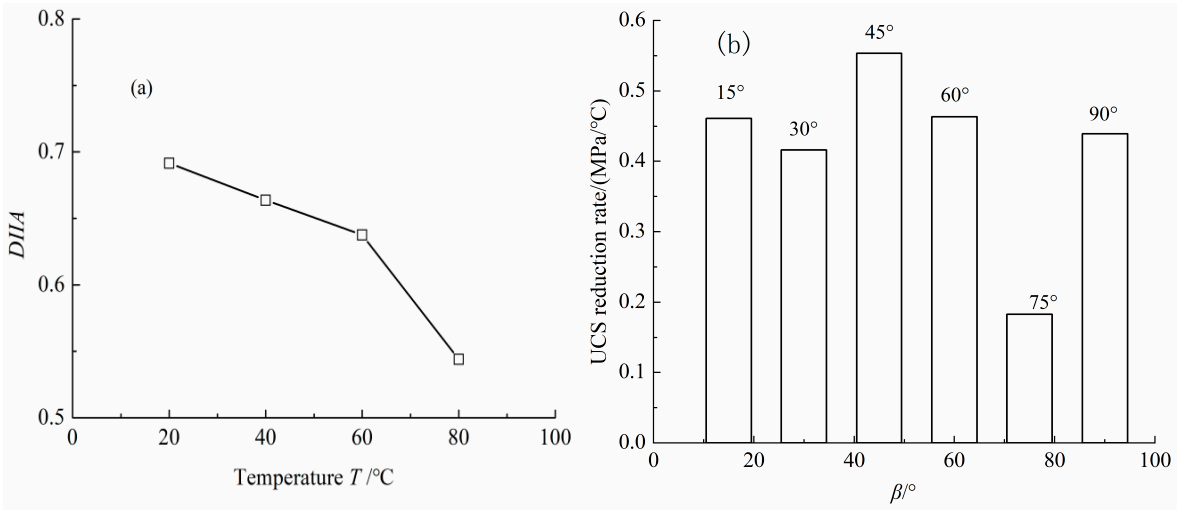


Figure 11. Influences of β and T on the UCS of composite specimens: (**a**) *DIIA* variation as a function of T and (**b**) variation of the UCS change rate as a function of β.

The average rate of change in the UCS for composite specimens with different β values as T increased is shown in Figure 11b. The change rates were relatively larger when β was 45° or 60°, indicating that these specimens were sensitive to temperature; this was primarily a result of the shear failure along their interfaces. At lower T values, the effects of temperature change on the composite specimen UCS were relatively minor and can be neglected. Considering the variations of the composite and concrete-only specimen UCS values with T, the impact of T on the UCS of the composite specimens was primarily related to the performance of the interface, whereas changes in the strength of the concrete itself did not alter the overall UCS trend.

The results of these analyses indicate that the UCS of the specimens first decreased and then increased as the β value increased; this change occurred at approximately 60°. In addition, the UCS gradually decreased at increasing T. Based on these trends, a predictive model for the UCS of the rock–concrete composite was established as follows:

$$\sigma_c^{T,\beta} = \begin{cases} \sigma_c^{20,60}[1 - m(T-20)] + a^{-60} - a^{-\beta} & 0° \le \beta \le 60° \\ \sigma_c^{T,60}\left[1 + K_{(T)}(\beta - 60)\right] & 60° < \beta \le 90° \end{cases} \quad (2)$$

where $\sigma_c^{T,\beta}$ is the UCS of the composite at β and T; $\sigma_c^{20,60}$ is the UCS of the composite at a T = 20 °C and β = 60°; m reflects the temperature-induced degradation of the material's uniaxial strength at the same β; a reflects how the UCS varies with β at T; and $K(T)$ indicates the rate of increase in UCS when β increases from 60° to 90° as a function of T.

Equation (2) was used to perform a nonlinear regression analysis on the UCS test results obtained in this study at different β and T values, as shown in Figure 12a. The regression results were applied to transform the model correlating the UCS of the composite with β and T into

$$\sigma_c^{T,\beta} = \begin{cases} \sigma_c^{20,60}[1 - 0.01343\cdot(T-20)] + 0.94^{-60} - 0.94^{-\beta} & 0° \le \beta \le 60° \\ \sigma_c^{T,60}[1 + 0.00146T(\beta - 60)] & 60° < \beta \le 90° \end{cases} \quad (3)$$

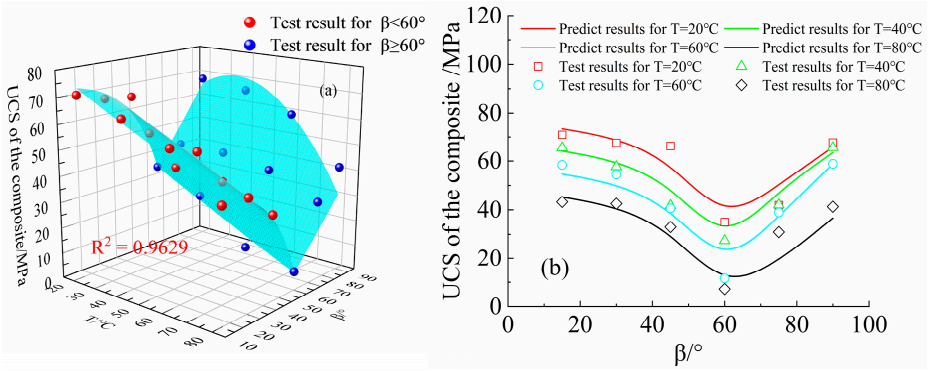


Figure 12. UCS prediction model for rock–concrete composites: (**a**) nonlinear regression analysis and (**b**) comparative verification.

A comparison between the results predicted by the model in Equation (3) and the experimental results obtained in this study is shown in Figure 12b. As shown, the model-predicted results closely match the experimental results, showing a maximum relative error of approximately 9.8% and confirming that the model derived in this study is reliable.

5. Conclusions

The mechanical properties and failure mechanisms of rock–concrete composite specimens were investigated in this study using uniaxial compression tests and AE monitoring to determine the influence of inclined interface angle (β) and geothermal temperature (T) on compressive strength and failure modes. The key conclusions drawn from this investigation are as follows:

(1) The uniaxial compressive stress–strain curves of the composite specimens exhibited four distinct stages: initial compression, linear elasticity, yielding, and post-peak. The post-peak stress–strain curve exhibited three basic types: stress fluctuation, stress drop, and post-peak hardening.

(2) The UCS of the composite decreased with increasing T. This is mainly due to the proportion of small-scale crack development within the composite specialties increasing

at increasing T. The increase in temperature makes the rock–concrete composite more susceptible to damage.

(3) The degree of influence of the inclined interface angle decreases with increasing temperature, indicating that environmental temperature can significantly reduce the influence of interface inclination.

(4) Specimens with $\beta = 60^{\circ}$ tended to exhibit a relatively higher proportion of large-scale cracks during failure than the other specimens and were more prone to failure under the same stress conditions. The failure modes of the rock–concrete composite specimens include axial penetration splitting, interface shear, Y-shaped fracture, and interface splitting-concrete shear failure.

(5) The observed variations in the UCS of the rock–concrete composite specimens with β and T were applied to develop a model correlating these characteristics. The results predicted by the present model matched the experimental data well, indicating suitable predictive performance.

Author Contributions: S.L.: data curation, formal analysis, and writing—original draft. J.Z.: conceptualization, supervision, and writing—review and editing. F.C.: funding acquisition and methodology. H.Y.: writing—original draft. J.C.: software. All authors have read and agreed to the published version of the manuscript.

Funding: This work was financed by the Special Fundamental Research Project of Hebei Natural Science Foundation (grant numbers E2021402023 and E2024402061), the Open Subject of the State Key Laboratory of Geotechnical Mechanics and Engineering, Institute of Rock and Soil Mechanics, Chinese Academy of Sciences (grant number Z018022), and by the Funded by Science and Technology Project of Hebei Education Department (grant numbers BJ2019023).

Data Availability Statement: The research data in this paper can be obtained by contacting the corresponding author.

Conflicts of Interest: The authors declare no conflicts of interest. The authors declare that they have no known competing financial interests or personal relationships that could have appeared to have influenced the work reported in this paper.

References

1. Fishman, Y.A. Stability of concrete retaining structures and their interface with rock foundations. *Int. J. Rock Mech. Min. Sci.* **2009**, *46*, 957–966. [CrossRef]
2. He, S.Y.; Lai, J.X.; Zhong, Y.J.; Wang, K.; Xu, W.; Wang, L.X.; Liu, T.; Zhang, C.P. Damage behaviors, prediction methods and prevention methods of rockburst in 13 deep traffic tunnels in China. *Eng. Fail. Anal.* **2021**, *121*, 105178. [CrossRef]
3. Smaniotto, S.; Neuner, M.; Dummer, A.; Cordes, T.; Hofstetter, G. Experimental study of a wet mix shotcrete for primary tunnel linings-Part I: Evolution of strength, stiffness and ductility. *Eng. Fract. Mech.* **2022**, *267*, 108409. [CrossRef]
4. Chen, Y.; Li, M.H.; Zhou, L.; Deng, L.T.; Wang, J.H. Effects of Different Loading Angles on Brazilian Splitting Characteristics of Rock-Concrete Interface. *Geotech. Geol. Eng.* **2024**, *42*, 4285–4301. [CrossRef]
5. Zhao, J.; Gong, Q.M.; Eisensten, Z. Tunnelling through a frequently changing and mixed ground: A case history in Singapore. *Tunn. Undergr. Space Technol.* **2007**, *22*, 388–400. [CrossRef]
6. Haas, M.; Mongeard, L.; Ulrici, L.; D'Aloia, L.; Cherrey, A.; Galler, R.; Benedikt, M. Applicability of excavated rock material: A European technical review implying opportunities for future tunnelling projects. *J. Clean. Prod.* **2021**, *315*, 128049. [CrossRef]
7. van Eldert, J.; Schunnesson, H.; Johansson, D.; Saiang, D. Application of Measurement While Drilling Technology to Predict Rock Mass Quality and Rock Support for Tunnelling. *Rock Mech. Rock Eng.* **2020**, *53*, 1349–1358. [CrossRef]
8. Gutiérrez-Ch, J.G.; Senent, S.; Melentijevic, S.; Jimenez, R. Distinct element method simulations of rock-concrete interfaces under different boundary conditions. *Eng. Geol.* **2018**, *240*, 123–139. [CrossRef]
9. Mouzannar, H.; Bost, M.; Leroux, M.; Virely, D. Experimental Study of the Shear Strength of Bonded Concrete-Rock Interfaces: Surface Morphology and Scale Effect. *Rock Mech. Rock Eng.* **2017**, *50*, 2601–2625. [CrossRef]
10. Zhao, H.; Hou, J.C.; Zhang, L.; Zhao, M.H. Towards concrete-rock interface shear containing similar triangular asperities. *Int. J. Rock Mech. Min. Sci.* **2021**, *137*, 104547. [CrossRef]

11. Zhong, H.; Ooi, E.T.; Song, C.M.; Ding, T.; Lin, G.; Li, H.J. Experimental and numerical study of the dependency of interface fracture in concrete-rock specimens on mode mixity. *Eng. Fract. Mech.* **2014**, *124*, 287–309. [CrossRef]
12. Zhang, M.C.; Sheng, Q.; Cui, Z. Experimental and numerical study on the mechanical properties of the rock-concrete contact surface for consideration of ground-liner interaction in rock tunnelling. *Eur. J. Environ. Civ. Eng.* **2023**, *27*, 339–355. [CrossRef]
13. Zheng, Y.L.; Zhang, Q.B.; Zhao, J. Challenges and opportunities of using tunnel boring machines in mining. *Tunn. Undergr. Space Technol.* **2016**, *57*, 287–299. [CrossRef]
14. Wang, Q.; Geng, P.; Li, P.S.; Wang, T.Q.; Sun, W.H. Failure analysis and dislocation-resistant design parameters of mining tunnel under normal faulting. *Eng. Fail. Anal.* **2023**, *143*, 106902. [CrossRef]
15. Lv, Y.; Shen, Y.J.; An, L.; Wei, X.; Chen, X.; He, R.J.; Shi, B.L.; Zhou, Z.H. A novel cement-based interface functional material for application onto shotcrete-rock interface of tunnel in cold regions. *Constr. Build. Mater.* **2024**, *438*, 136923. [CrossRef]
16. Simanjuntak, T.; Marence, M.; Schleiss, A.J.; Mynett, A.E. The Interplay of In Situ Stress Ratio and Transverse Isotropy in the Rock Mass on Prestressed Concrete-Lined Pressure Tunnels. *Rock Mech. Rock Eng.* **2016**, *49*, 4371–4392. [CrossRef]
17. Fang, H.C.; Zhang, D.L.; Fang, Q. A semi-analytical method for frictional contact analysis between rock mass and concrete linings. *Appl. Math. Model.* **2022**, *105*, 17–28. [CrossRef]
18. Tao, Y.X.; Ren, Q.; Vantyghem, G.; Lesage, K.; Van Tittelboom, K.; Yuan, Y.; De Corte, W.; De Schutter, G. Extending 3D concrete printing to hard rock tunnel linings: Adhesion of fresh cementitious materials for different surface inclinations. *Autom. Constr.* **2023**, *149*, 104787. [CrossRef]
19. Fang, X.Q.; Ma, H.W.; Zhu, C.S.; Ding, Q.L.; Zhu, Z.G.; Han, Z.M. Imperfect interface model and dynamic interaction mechanism around tunnels under seismic waves: A review. *Tunn. Undergr. Space Technol.* **2023**, *137*, 105120. [CrossRef]
20. Krounis, A.; Johansson, F.; Larsson, S. Shear Strength of Partially Bonded Concrete-Rock Interfaces for Application in Dam Stability Analyses. *Rock Mech. Rock Eng.* **2016**, *49*, 2711–2722. [CrossRef]
21. Moradian, Z.A.; Ballivy, G.; Rivard, P. Application of acoustic emission for monitoring shear behavior of bonded concrete-rock joints under direct shear test. *Can. J. Civ. Eng.* **2012**, *39*, 887–896. [CrossRef]
22. Bost, M.; Mouzannar, H.; Rojat, F.; Coubard, G.; Rajot, J.P. Metric Scale Study of the Bonded Concrete-Rock Interface Shear Behaviour. *KSCE J. Civ. Eng.* **2020**, *24*, 390–403. [CrossRef]
23. Bista, D.; Sas, G.; Johansson, F.; Lia, L. Influence of location of large-scale asperity on shear strength of concrete-rock interface under eccentric load. *J. Rock Mech. Geotech. Eng.* **2020**, *12*, 449–460. [CrossRef]
24. Dong, W.; Wu, Z.M.; Zhou, X.M. Fracture Mechanisms of Rock-Concrete Interface: Experimental and Numerical. *J. Eng. Mech.* **2016**, *142*, 105120. [CrossRef]
25. Zhou, Z.L.; Lu, J.Y.; Cai, X. Static and dynamic tensile behavior of rock-concrete bi-material disc with different interface inclinations. *Constr. Build. Mater.* **2020**, *256*, 119424. [CrossRef]
26. Guo, T.F.; Liu, K.W.; Ma, S.Z.; Yang, J.C.; Li, X.; Zhou, K.F.; Qiu, T. Dynamic fracture behavior and fracture toughness analysis of rock-concrete bi-material with interface crack at different impact angles. *Constr. Build. Mater.* **2022**, *356*, 129286. [CrossRef]
27. Wu, D.Y.; Su, H.J.; Yu, L.Y.; Zhang, F.L.; Qin, H.; Wei, C.; Geng, S.T. Experimental and numerical investigation of dynamic tensile behavior of granite-concrete bimaterials with different rough interfaces. *J. Build. Eng.* **2024**, *84*, 108565. [CrossRef]
28. Zhang, C.; Zhu, Z.D.; Wang, S.Y.; Zhang, Y.G. Experimental Research on Dynamic Failure of Rock-Cemented Material-Rock Interface Considering Strain Rate Effect. *Rock Mech. Rock Eng.* **2024**, *57*, 145–162. [CrossRef]
29. Saiang, D.; Malmgren, L.; Nordlund, E. Laboratory tests on shotcrete-rock joints in direct shear, tension and compression. *Rock Mech. Rock Eng.* **2005**, *38*, 275–297. [CrossRef]
30. Zhao, B.Y.; Liu, Y.; Liu, D.Y.; Huang, W.; Wang, X.P.; Yu, G.B.; Liu, S. Research on the influence of contact surface constraint on mechanical properties of rock-concrete composite specimens under compressive loads. *Front. Struct. Civ. Eng.* **2020**, *14*, 322–330. [CrossRef]
31. Selçuk, L.; Asma, D. Experimental investigation of the Rock-Concrete bi materials influence of inclined interface on strength and failure behavior. *Int. J. Rock Mech. Min. Sci.* **2019**, *123*, 104119. [CrossRef]
32. Xu, H.; Zhang, Z.; Yan, J.; Jiang, Z.P.; Zhao, L.S.; Zhang, Y.J. Study on mechanical properties and failure mechanism of hard rock with stiff discontinuities based on 3D printing. *Eng. Fail. Anal.* **2024**, *161*, 108225. [CrossRef]
33. Wu, W.; Xu, W.B.; Zuo, J.P. Effect of inclined interface angle on shear strength and deformation response of cemented paste backfill-rock under triaxial compression. *Constr. Build. Mater.* **2021**, *279*, 122478.
34. Shen, M.X.; Zhao, Y.; Bi, J.; Wang, C.L.; Du, B. Microstructure evolution and damage mechanisms of concrete-rock-composite corrosion in acid environment. *J. Build. Eng.* **2024**, *82*, 108336. [CrossRef]
35. Dong, Z.; Lin, T.R.; Tang, S.B.; Lang, Y.X.; Yuan, R.F.; Heng, S. Mechanical properties and failure mechanism of concrete-granite composite specimens under compression load. *Constr. Build. Mater.* **2024**, *435*, 136768. [CrossRef]
36. Wilhelm, J.; Rybach, L. The geothermal potential of Swiss Alpine tunnels. *Geothermics* **2003**, *32*, 557–568. [CrossRef]
37. Hochstein, M.P.; Prebble, W.M. Major engineering constructions on top of a high-temperature geothermal system: Problems encountered at Tokaanu, New Zealand. *Geothermics* **2006**, *35*, 428–447. [CrossRef]

38. Xie, J.T.; Yu, Y.Y. Grades for Heat Damage in High Altitude Tunnel Engineering. *J. Railw. Eng. Soc.* **2013**, *30*, 69–73.
39. Wang, M.N.; Hu, Y.P.; Wang, Q.L.; Tian, H.T.; Liu, D.G. A study on strength characteristics of concrete under variable temperature curing conditions in ultra-high geothermal tunnels. *Constr. Build. Mater.* **2019**, *229*, 116989. [CrossRef]
40. Guo, T.F.; Liu, K.W.; Li, X.; Wu, Y.; Yang, J.C. Effects of thermal treatment on the fracture behavior of rock-concrete bi-material specimens containing an interface crack. *Theor. Appl. Fract. Mech.* **2023**, *127*, 104071. [CrossRef]
41. Shen, Y.J.; Wang, Y.Z.; Yang, Y.; Sun, Q.; Luo, T.; Zhang, H. Influence of surface roughness and hydrophilicity on bonding strength of concrete-rock interface. *Constr. Build. Mater.* **2019**, *213*, 156–166. [CrossRef]
42. Tahwia, A.M.; Aldulaimi, D.S.; Abdellatief, M.; Youssef, O. Physical, Mechanical and Durability Properties of Eco-Friendly Engi-neered Geopolymer Composites. *Infrastructures* **2024**, *9*, 191. [CrossRef]
43. Tang, Y.; Xu, G.B.; Lian, J.J.; Su, H.; Qu, C.L. Effect of temperature and humidity on the adhesion strength and damage mechanism of shotcrete-surrounded rock. *Constr. Build. Mater.* **2016**, *124*, 1109–1119. [CrossRef]
44. Fang, K.; Fall, M. Effects of curing temperature on shear behaviour of cemented paste backfill-rock interface. *Int. J. Rock Mech. Min. Sci.* **2018**, *112*, 184–192. [CrossRef]
45. Tong, J.; Karakus, M.; Wang, M.; Dong, C.; Tang, X. Shear strength characteristics of shotcrete–rock interface for a tunnel driven in high rock temperature environment. *Geomech. Geophys. Geo-Energy Geo-Resour.* **2016**, *2*, 331–341. [CrossRef]
46. Zhang, Y.C.; Huang, M.; Jiang, Y.J.; Wang, Z. Mechanics, damage and energy degradation of rock-concrete interfaces exposed to high temperature during cyclic shear. *Constr. Build. Mater.* **2023**, *405*, 133229. [CrossRef]
47. Su, H.J.; Wang, W.B.; Yu, L.Y.; Nie, Y.J.; Zhang, L.Q.; Liu, J.W. Uniaxial Compressive Behaviors of Sandstone-concrete Binary with Rough Interface after High Temperatures. *KSCE J. Civ. Eng.* **2024**, *28*, 3543–3557. [CrossRef]
48. *JGJ 55–2011*; Specification for Mix Proportion Design of Ordinary Concrete. Ministry of Housing and Urban-Rural Development of The People's Republic of China: Beijing, China, 2011. (In Chinese)
49. *ASTM D2938-95*; Standard Test Method for Unconfined Strength of Intact Rock Core Specimens. ASTM International: West Conshohocken, PA, USA, 2000.
50. *ASTM D4543-19*; Standard Practices for Preparing Rock Core as Cylindrical Test Specimens and Verifying Conformance to Dimensional and Shape Tolerances. ASTM International: West Conshohocken, PA, USA, 2019.
51. Zhang, Q.; Zhang, X.P. A numerical study on cracking processes in limestone by the b-value analysis of acoustic emissions. *Comput. Geotech.* **2017**, *92*, 1–10. [CrossRef]
52. Colombo, I.S.; Main, I.G.; Forde, M.C. Assessing the damage of reinforced concrete beam using "b-value" analysis of acoustic emission signals. *J. Mater. Civ. Eng.* **2003**, *15*, 280–286.
53. Zhang, Z.P.; Zhang, R.; Xie, H.P.; Liu, J.F.; Were, P. Differences in the acoustic emission characteristics of rock salt compared with granite and marble during the damage evolution process. *Environ. Earth Sci.* **2015**, *73*, 6987–6999.
54. Zhang, Z.B.; Liu, X.N.; Zhang, Y.H.; Qin, X.Y.; Khan, M. Comparative study on fracture characteristics of coal and rock samples based on acoustic emission technology. *Theor. Appl. Fract. Mech.* **2021**, *111*, 102851. [CrossRef]
55. Ge, Z.L.; Sun, Q. Acoustic emission (AE) characteristics of granite after heating and cooling cycles. *Eng. Fract. Mech.* **2018**, *200*, 418–429. [CrossRef]

Disclaimer/Publisher's Note: The statements, opinions and data contained in all publications are solely those of the individual author(s) and contributor(s) and not of MDPI and/or the editor(s). MDPI and/or the editor(s) disclaim responsibility for any injury to people or property resulting from any ideas, methods, instructions or products referred to in the content.